Physical characterization and in vitro evaluation of 3D printed hydroxyapatite, tricalcium phosphate, zirconia, alumina, and SiAlON structures made by lithographic ceramic manufacturing

Authors: Alexander K. Nguyen[1,2], Peter L. Goering[2], Shelby A. Skoog[2], Roger J. Narayan[1*]

Affiliations:

[1] Joint UNC/NCSU Department of Biomedical Engineering, North Carolina State University, Raleigh, North Carolina, United States

[2] Center for Devices and Radiological Health, U.S. Food and Drug Administration, Silver Spring, MD

Abstract:

In this study, lithographic ceramic manufacturing was used to create solid chips out of hydroxyapatite, tricalcium phosphate, zirconia, alumina, and SiAlON ceramic. X-ray powder diffraction of each material confirmed that the chips were crystalline, with little amorphous character that could result from remaining polymeric binder, and were composed entirely out of the ceramic feedstock. Surface morphologies and roughnesses were characterized using atomic force microscopy. Human bone marrow stem cells cultured with osteogenic supplements on each material type expressed alkaline phosphatase levels, an early marker of osteogenic differentiation, on par with cells cultured on a glass control. However, cells cultured on the tricalcium phosphate-containing material expressed lower levels of ALP suggesting that osteoinduction was impaired on this material. Further analyses should be conducted with these materials to identify underlying issues of the combination of material and analysis method.

INTRODUCTION:

As noted by Schwentenwein et al., ceramic parts created by conventional 3D printing approaches such as selective laser sintering often suffer from insufficient densities and poor mechanical properties [1]. A vat photopolymerization-based 3D printing approach known as lithographic ceramic manufacturing (LCM) from Lithoz GmbH (Vienna, Austria) has been developed to 3D print bioceramic parts [2]. Unlike other 3D printing approaches, vat polymerization-based 3D printing methods are known for providing parts with superior mechanical properties and surface quality, a high level of precision and homogeneity, and isotropic microstructure [3].

In LCM, the photoactive slurry is solidified in a layer-by-layer manner by exposure to blue light from a light emitting diode, which is patterned by a digital micromirror device. The photoactive slurry used in LCM includes a ceramic powder with particle size in the range of 0.01-50 μm, which is uniformly dispersed in a matrix containing a commercial acrylate- or methacrylate-based monomer, nonreactive organic diluents, dispersing agent, organic solvent, inert light absorber, and photoinitiator.

Unlike many other 3D printing approaches, the part in LCM is built in an "upside-down" orientation. The "upside down" build orientation significantly reduces the amount of slurry that is used in the 3D printing process. Since nearly all of the precursor material that is fed into the instrument is solidified, the LCM process is efficient in terms of resource utilization and cost [3].

The 3D printing process involves the following steps: (a) a thin layer of photoactive slurry is coated on the transparent vat, (b) the building platform approaches the vat, leaving a micrometer-level gap for the photoactive slurry, (c) a recoating system that includes a static wiper blade and a rotating vat is used to spread a fresh layer of the photoactive slurry and create a thin slurry film, and (d) a pattern of blue LED light from the digital micromirror device is used to selectively polymerize regions of the photoactive slurry layer. Since the bottom of the vat is transparent, a light source can illuminate the photoactive slurry through the rotating vat from below. The cured layer then becomes attached to the building platform. The building platform, which is located above the vat, subsequently moves upwards to polymerize the next layer of photoactive slurry. The steps mentioned above are repeated until the 3D printing process is completed.

The resulting green body is a composite that consists of ceramic particles held together by the photoactive polymer matrix [4]. This part is then cleaned with pressurized air and LithaSol 20 (Lithoz GmbH, Vienna, Austria) solvent, which dissolves the slurry without damaging the photopolymerized part. After cleaning, the green part then undergoes a conventional ceramic forming thermal treatment to (a) remove the solvent, (b) decompose the

polymeric binder, as well as (c) densify and sinter the remaining material. The thermal treatment leaves no residual organic component in the 3D printed parts. After the thermal treatment, the 3D printed part exhibits high density, high strength, and similar mechanical properties to ceramic parts made from powder precursors using conventional approaches [3]. For example, zirconia parts made by LCM show high density (>99.8 % relative density) [3]. Other benefits of the LCM process include the ability to prepare implants with complex shapes otherwise impossible with other fabrication methods (e.g., CNC milling), and high geometric fidelity to the initial design. LCM is able to fabricate structures with geometries similar to orthopedic implants that are commonly fabricated using stereolithography [5-7]; with LCM, the structures can be created out of clinically-used ceramics. Several researchers have previously examined medical applications for LCM technology. For example, Chen et al. showed that tricalcium phosphate (TCP)-based scaffolds successfully regenerated bone and bridged a bony defect over four weeks in a noncritical-size defect that was created in a rabbit calvarium [2]. However, the conventionally-produced titanium scaffold showed better functionality and mechanical stability versus the TCP scaffold for a critical-size defect [2]. Ghayor and Weber showed that 3D printed TCP scaffolds in a rabbit calvarial bone defect model provided optimal osteoconductivity with pore diameters between 0.7-1.2 mm and bottlenecks between 0.5-1.2 mm [4].

The objective of this study was to evaluate additional LCM materials for potential use in orthopedic devices. LCM was used to create 10 mm diameter chips with a thickness of 1.5 mm out of various ceramic materials. X-ray diffraction was used to evaluate the composition of the materials. *In vitro* assays were performed with commercially-obtained human bone marrow-derived stem cells cultured on the LCM chips and in the presence of osteogenic supplements; alkaline phosphatase (ALP) levels, an early marker of osteogenic differentiation, were assessed to detect any effect on osteogenic differentiation.

METHODS:

LCM Chip Processing and Sterilization

LCM of 10 mm diameter, 1.5 mm thick chips of eight different Lithoz materials where the primary ceramic components were 1) alumina-toughened zirconia (ATZ), 2) 3 mol% yttria-stabilized zirconia (3YSZ), 3) zirconia-toughened alumina (ZTA), 4) 99.99% purity aluminum oxide (Al_2O_3 99.99%), 5) 99.8% purity aluminum oxide (Al_2O_3 99.8%), 6) SiAlON, 7) hydroxyapatite (HA), and 8) TCP (Lithoz GmbH, Vienna, Austria) was performed as described previously [1, 3]. In brief, a ceramic slurry composed primarily of ceramic particles (typically 75 – 85%

w/w) and a liquid methacrylate-based photocrosslinkable resin were additively manufactured on a CeraFab 7500 lithography ceramic manufacturing printer (Lithoz GmbH, Vienna, Austria). A LED light engine coupled with a digital micromirror chip projects a cross-section of the object onto the bottom of a photopolymer vat, adhering the layer onto the build platform. Subsequent layers are produced by peeling the build platform off the bottom, blade coating additional slurry, then contacting the structure to the vat bottom before additional illumination takes place. The ceramic green body is heated in a debinding furnace to 900 ^{0}C to remove the acrylate component, then sintered at a temperature between 1300-1750 °C (depending on the requirements of the different ceramics) to produce the final structure.

Physical Characterization

X-ray diffraction (XRD) analysis was used to determine the chemical composition and crystal structure of each ceramic type by peak-matching with reference spectra from the International Centre for Diffraction Data (ICDD) Powder Diffraction File (PDF) database. All samples were scanned from $2\theta = 0$ to 90^0 on a Panalytical Empyrean X-ray Diffractometer (Malvern PANalytical, Royston, UK) using Cu K-α1 X-ray radiation. Signal was collected using a 0.026 degree step size at 96 sec per step. XRD spectra were matched with reference spectra in the ICDD PDF4+ database (ICDD, Newtown Square, PA) using the HighScore Plus software (Malvern PANalytical, Royston, UK). The topography of each sample was imaged on an Asylum MFP-3D (Asylum Research, Morrisville, NC) Atomic Force Microscope. In the AFM analysis, 10x10 μm and 2x2 μm regions were scanned using 256 scan lines measuring at 256 points per line at a 0.75 Hz scan rate.

Cell Culture

Nine chips of each material type and 18 x 10 mm square borosilicate glass coverslips were washed 2x in isopropanol for 2 minutes per wash, 1x in acetone, and then autoclaved before biological assays. Human bone marrow-derived stem cells (hBMSC) were cultured in mesenchymal stem cell basal medium with the bone marrow-derived mesenchymal stem cell growth kit (ATCC, Manassas, VA). hBMSC at passage 5 were seeded at a density of 3.1×10^4 cells/cm^2 on the ceramic chips and glass coverslips; ATCC recommends passage 6 as the maximum passage for osteogenic differentiation procedures. All samples were incubated for 4 hr for cell attachment before the media was replaced with the Osteocyte Differentiation Tool (PCS-500-052, ATCC, Manassas, VA) which are media containing osteogenic supplements (OS). Samples were incubated at 37 ^{0}C, 5% CO_2, and 95% humidity.

Collection of Cell Lysate for PicoGreen® and ALP Liquicolor® Assays

During days 7, 14, and 21, samples were removed from the plate, rinsed 3x in excess PBS, and placed into a new 24-well plate to minimize interference from cells attached to the plate surfaces and from serum in the cell culture medium. hBMSC were lysed in 0.5 mL of 0.2% w/w Triton X-100 (Sigma Aldrich, St. Louis, MO) in ultrapure water (>18.2 MΩ·cm; Millipore, St. Louis, MO) for 30 minutes on a shaker. The resulting cell lysate was used immediately in both the PicoGreen® dsDNA assay (Thermo Fisher Scientific, Waltham, MA) and the Alkaline Phosphatase Liquicolor® assay (EKF Diagnostics, Boerne, TX).

Cell lysate generated from a solution of known cell density was produced to correlate dsDNA content in this assay to cell number. hBMSC were trypsinized (Sigma Aldrich, St. Louis, MO) and centrifuged at 200 x g for 5 minutes and the supernatant discarded. The pellet was resuspended in 10 mL of ultrapure water and the cell density was measured to be 2.16×10^5 cells/mL. Triton X-100 was added to produce a 0.2% w/w solution and then the solution was agitated for 30 minutes. Cell lysate was aliquoted and stored at -70^0C until use for the cell ladder control. For each timepoint, cell lysate was diluted in appropriate volumes of 0.2% Triton X-100 to produce 8 solutions ranging from 0 to 1.0×10^5 cells/mL.

Cell lysate (50 μL) from hBMSC cultured on the 8 materials, glass control without osteogenic supplements (OS-), glass control with osteogenic supplements (OS+), and 8 cell ladder solutions were transferred in triplicate to a 96-well plate. PicoGreen® dye working solution (50 μL) in TE buffer (Quality Biological Inc., Gaithersburg, MD) was added to each well and stained for at least 5 minutes before reading in a fluorescence plate reader at 480 nm and 500 nm excitation and emission wavelengths respectively. Final concentrations of Triton X-100 would be 0.1% in all wells during staining which is the maximum acceptable concentration for the PicoGreen® assay as specified by the manufacturer.

For the ALP assay, SER-T-FY Level 1 Control Serum (EKF Diagnostics Inc., Boerne, TX) from lot 24474 was rehydrated in 5.000 g of ultrapure water on an analytical balance. Serum was diluted 1:1 with 0.4% Triton X-100 in ultrapure water as the serum control containing 48 U/L ALP. Cell lysate (50 μL) from the 8 materials, OS- glass control, OS+ glass control, 50 μL of the serum solution, and blank 0.2% Triton X-100 were transferred in triplicate to a 96-well plate. Liquicolor® dye solution (50 μL) was added and immediately measured in a plate reader using absorbance at 405 nm four times per minute for 15 minutes. The change in absorbance over time was correlated to the change in serum control wells to calculate the ALP activity of lysate from each sample.

For cell lysate from each sample, the ALP activity measured by the ALP Liquicolor® assay was normalized to cell count determined by the PicoGreen® assay. Three independent replicates were performed and the detection of

ALP expression increase was determined by comparing the normalized ALP signal for cell lysate from each sample versus the signal from the corresponding OS- and OS+ glass controls for that timepoint using a two-tailed Student's t-test; results were deemed statistically significant at the $p < 0.05$ level.

RESULTS & DISCUSSION:

XRD spectra of each ceramic material are presented in Figure 1. ATZ, 3YSZ, and ZTA all contained tetragonal ZrO_2 (Powder Diffraction File# 00-050-1089). ATZ, ZTA, Al_2O_3 99.99%, and Al_2O_3 99.8% contained α-Al_2O_3 (Powder Diffraction File# 04-007-4873). LithaNite 720 contained β-SiAlON [8, 9]. HA-MS8F and TCP-MS8F were HA (PDF# 04-014-8416) and TCP (Powder Diffraction File# 04-001-7220) respectively. All ceramics except for ATZ had excellent fits with their respective reference spectra in peak location and intensity. The β-SiAlON spectra agree with previous data collected on this material, including peaks at 29.5^0 and 31.1^0, which were attributed to Y2O3 and Si3N4 respectively [10]. A similar diffraction pattern is also identified in the Joint Committee on Powder Diffraction Standards (JCPDS) card 48-1615 as β-SiAlON [8] and more specifically as either Si_5AlON_7 or $Si_4Al_2O_2N_6$ [9]. Aluminum oxide peaks were present but almost undetectable in ATZ, suggesting a very low proportion of this material. XRD analysis confirms that all materials except for ZTA were primarily composed of a single crystalline material with low proportions of sintering aids; ZTA contains both tetragonal ZrO_2 and rhombohedral Al_2O_3 with no other detected peaks.

AFM images (Figure 2) of the ceramic materials revealed widely varying grain morphologies and surface roughness; composition and RMS roughness values for each ceramic are summarized in Table 1. The RMS roughness values from 10 x 10 μm and 2 x 2 μm regions of each material were measured from AFM data. ATZ and 3YSZ, both primarily yttria-stabilized zirconia, consisted of sub-micron grains and had similar RMS roughness when measured between the 10 μm and 2 μm regions.

ALP was measured as an early marker of osteogenic differentiation; ALP expression normalized to cell count is depicted in Figure 3. hBMSC exposed to osteogenic supplements and grown on any surface exhibited elevated ALP levels compared to hBMSC cultured on glass in the absence of osteogenic supplements. However, hBMSC cultured on some of the materials exhibited different ALP levels when compared to hBMSC cultured on glass in the presence of osteogenic supplements.

Compared to hBMSC cultured on glass and exposed to osteogenic supplements, hBMSC on ATZ had lower ALP expression on day 7 and 14 but was not significantly different by day 21. hBMSC on 3YSZ had lower ALP

expression on Day 14 although this timepoint had an outlier; statistics were calculated from N = 2 independent replicates instead of 3 as with all other groups. hBMSC on SiAlON had lower expression at Day 21 and TCP-MS8F had lowered ALP expression at all timepoints. Thus, most materials did not have a significant effect on hBMSC osteoinduction except for TCP-MS8F, the material composed of TCP. TCP is noted in the literature to be an osteoinductive material [11, 12] so other processes may be responsible for the drop in ALP expression.

One possible factor associated with reduced ALP expression for the TCP material could be the cleaning of the chips with isopropanol and acetone before sterilization, which may have remained after autoclaving. The TCP material may be more porous than the other materials and may have absorbed solvent. Acetone, in particular, may have effects on the bone marrow and may cause bone loss. Recent studies investigating the effects of a ketogenic diet have noted lower bone mineral content in rats, [13] mice, [14] and humans [15]; acetone is a metabolite generated during ketosis and can be used as a biomarker of ketoacidosis [16]. A study investigating the effects of acetone in drinking water noted bone marrow hypoplasia in rats dosed with high levels of acetone [17]. In this study, differences in surface morphology or porosity were not controlled, so it is possible that residual acetone from the cleaning process may have caused a drop in ALP expression.

ALP is linked with mineralization via multiple possible mechanisms such as the generation of inorganic phosphates for HA growth or the hydrolysis of pyrophosphates that inhibit HA growth [18]; areduction of this marker could have a negative effect on osseointegration of orthopedic implants. One example is a study by Bonsignore et al., which found that machine oil contamination of Ti-6Al-4V implants inhibited ALP expression among other osteogenic markers in MC3T3-E1 pre-osteoblasts; this finding was also associated with reduced bone-implant contact and pullout force in screws implanted in a murine model [19].

Surface roughness also affects ALP as a marker of osteogenic differentiation and could have played a role in ALP expression in this study. Faia-Torres et al. investigated the effects of surface roughness on osteogenic differentiation of human primary bone marrow stem cells on polycaprolactone substrates in the presence and absence of OS; R_a values around 2.1 – 3.1 μm [20] and 0.93 – 1.53 μm [21] determined using optical profilometry were found to increase ALP expression along with other markers of osteogenic differentiation. These roughness values may be underestimated compared to values measured using AFM [22]. Thus, the materials in this study with R_{rms} values one or two orders of magnitude lower than values determined by Faia-Torres et al. should be far under the optimal roughness; as such, roughness in this study should not be a significant factor in ALP expression.

No correlation between surface roughness measured from either the 10 μm or 2 μm area with ALP expression from a linear regression was observed with R^2 values of 0.06 and 0.19, respectively.

CONCLUSIONS:

LCM and subsequent sintering of additively manufactured ceramic parts yield pure crystalline ceramic parts with little evidence of residual polymeric binder and are highly similar to their respective feedstock material composition. When potentially applied to orthopedic implants, all tested materials except for TCP were found to not interfere with osteogenic differentiation. As TCP is known to be an osteoconductive material, an unidentified property of the finished TCP ceramic or steps during handling causes a drop in early osteogenic differentiation markers. Future work should be focused on determining the post-processing parameters and sterilization methods that have significant effects on osteoinduction.

ACKNOWLEDGEMENTS:

Martin Schwentenwein and Daniel Bomze from Lithoz GmbH for donating the LCM samples. Ching-Chang Chung and Charles Mooney from North Carolina State University Advanced Characterization Facility for expertise in XRD and AFM respectively. Funding for this project was provided by National Science Foundation Award #1762202.

DISCLAIMER:

The findings and conclusions in this paper have not been formally disseminated by the Food and Drug Administration and should not be construed to represent any agency determination or policy. The mention of commercial products, their sources, or their use in connection with material reported herein is not to be construed as either an actual or implied endorsement of such products by Department of Health and Human Services.

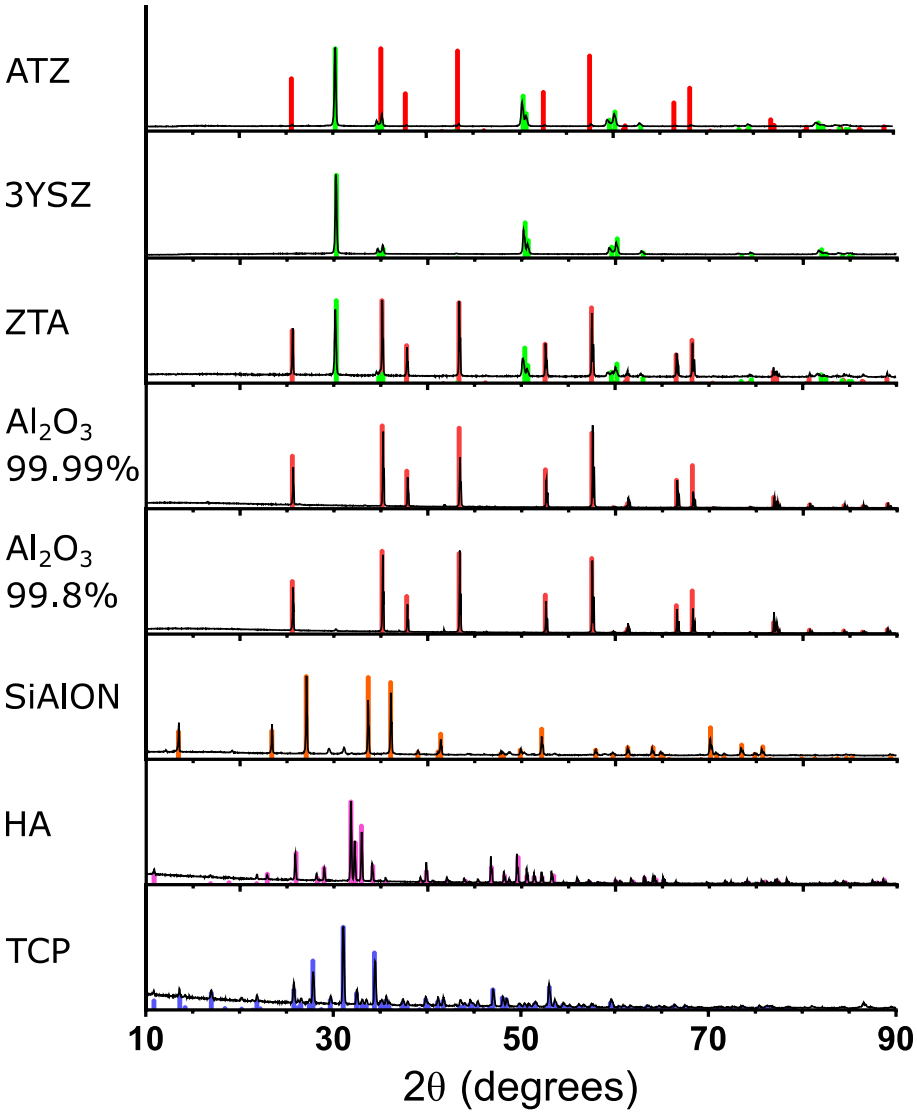

Figure 1 – XRD spectra (black line) of the LCM ceramics after sintering. Colored highlights correspond to the reference spectra of tetragonal zirconia (green, ZrO_2, Powder Diffraction File# 00-050-1089), alumina (red, α-Al_2O_3, Powder Diffraction File# 04-007-4873), silicon nitride (orange, β-Si_3N_4, Powder Diffraction File# 00-033-1160), HA (purple, $Ca_5(PO_4)_3(OH)$, Powder Diffraction File# 04-014-8416), and TCP (blue, $Ca_3(PO_4)_2$, Powder Diffraction File# 04-001-7220).

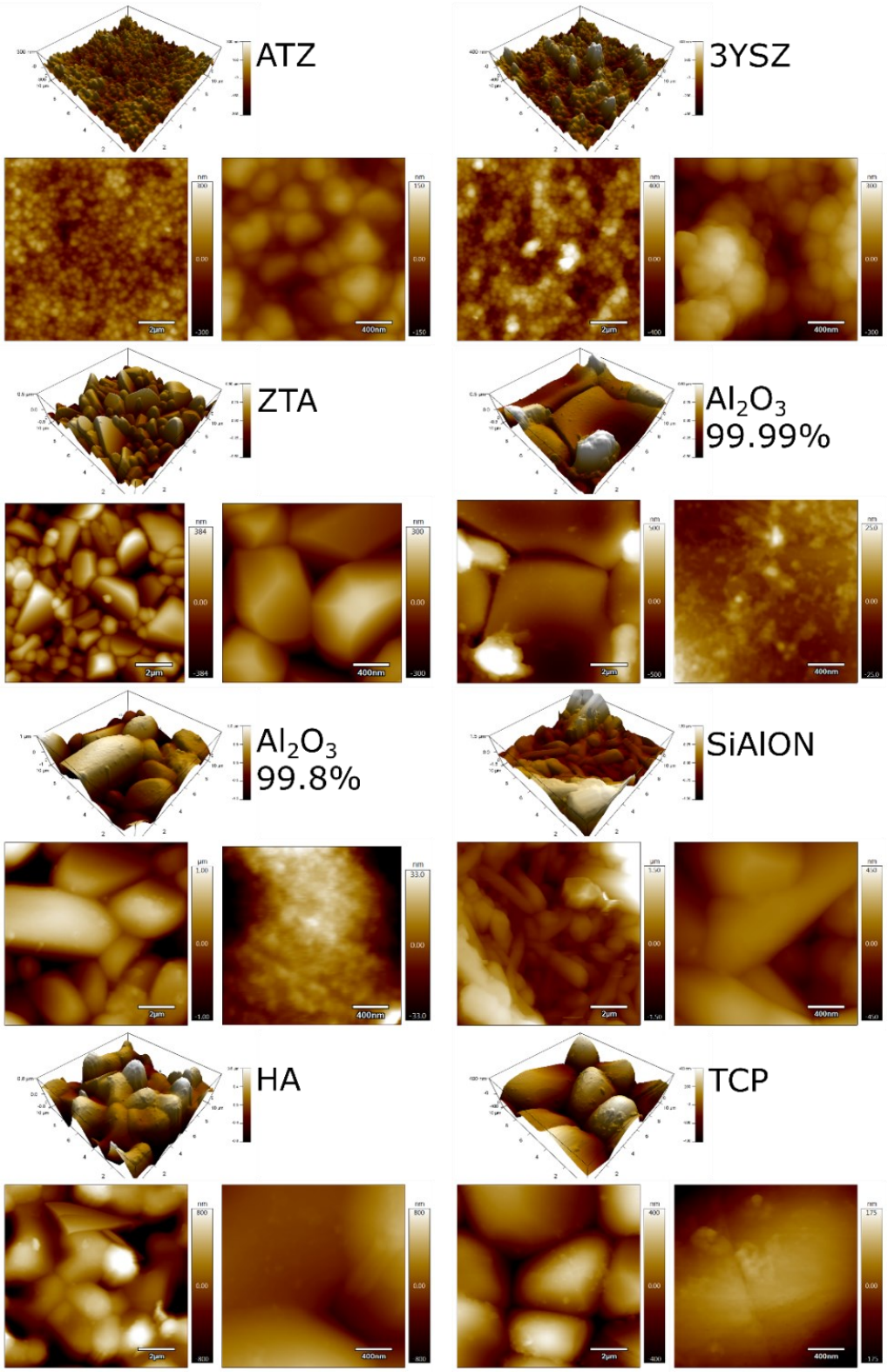

Figure 2 – 3D renderings and topographical maps from AFM data from the sintered LCM ceramics. Scale bars are 2 µm for the left image and 400 nm for the right image for each material. Roughness data is summarized in Table 1.

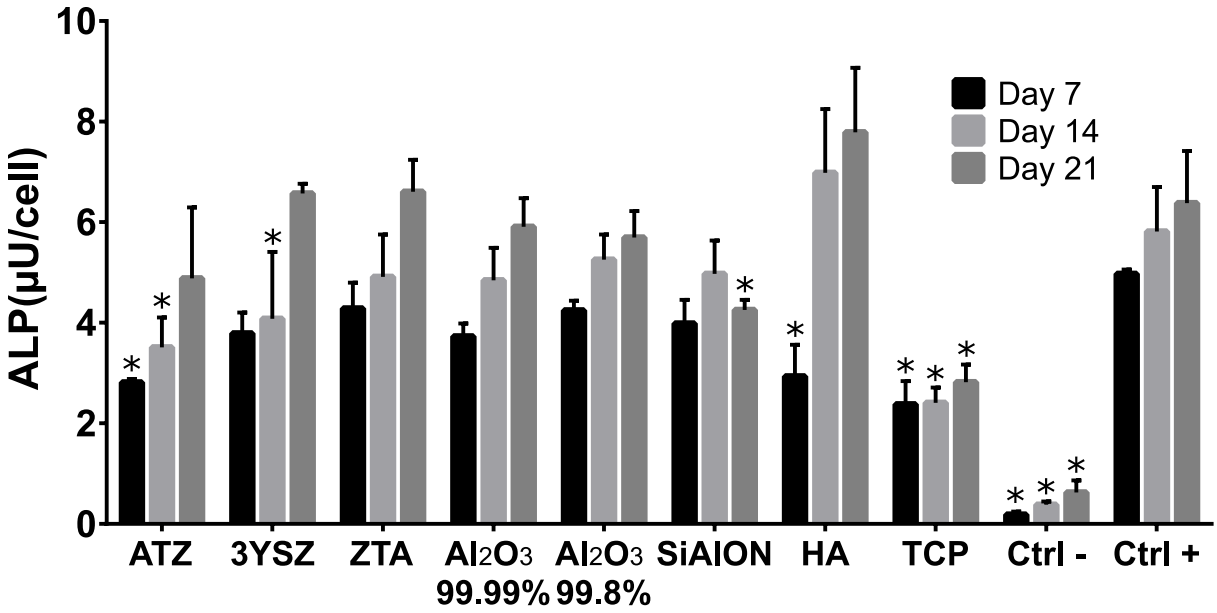

Figure 3 – ALP expression of hBMSC grown in the presence of osteogenic supplements and cultured on sintered LCM ceramics or glass and assayed at day 7 (black), day 14 (light gray), and day 21 (gray). ALP measured from the ALP Liquicolor® assay was normalized to cell count determined from the PicoGreen® assay. hBMSC cultured on borosilicate glass coverslips and grown in mesenchymal stem cell media and osteogenic media were used as the negative (Ctrl -) and positive (Ctrl +) controls respectively. Asterisks (*) represent values significantly different ($p < 0.05$) from the corresponding positive control at the same timepoint. Values represent the means and standard deviations of N = 3 independent replicates (except for ATZ day 14, which has N = 2).

Table 1 - Composition and RMS Roughness of Sintered LCM ceramics

Material	Identified phases	RMS Roughness (nm)	
		10x10 µm Area	2x2 µm Area
ATZ	t-ZrO_2	57	32
	α-Al_2O_3		
3YSZ	t-ZrO_2	111	104
ZTA	t-ZrO_2	483	105
	α-Al_2O_3		
Al_2O_3 99.99%	α-Al_2O_3	199	6
Al_2O_3 99.8%	α-Al_2O_3	489	17
SiAlON	β-Si_3N_4	604	120
HA	$Ca_5(PO_4)_3(OH)$	483	187
TCP	$Ca_3(PO_4)_2$	159	60

References:

1. Schwentenwein, M., P. Schneider, and J. Homa, *Lithography-Based Ceramic Manufacturing: A Novel Technique for Additive Manufacturing of High-Performance Ceramics.* Advances in Science and Technology, 2014. **88**: p. 60-64.
2. Chen, T.-H., et al., *Lattice Microarchitecture for Bone Tissue Engineering from Calcium Phosphate Compared to Titanium.* Tissue Engineering Part A, 2018. **24**(19-20): p. 1554-1561.
3. Bomze, D. and A. Ioannidis, *3D-Printing of High-Strength and Bioresorbable Ceramics for Dental and Maxillofacial Surgery Applications-the LCM Process.* Ceramic Applications, 2019. **7**(1): p. 38-43.
4. Ghayor, C. and F.E. Weber, *Osteoconductive Microarchitecture of Bone Substitutes for Bone Regeneration Revisited.* Frontiers in physiology, 2018. **9**: p. 960-960.
5. Kim, K., et al., *Stereolithographic Bone Scaffold Design Parameters: Osteogenic Differentiation and Signal Expression.* Tissue Engineering Part B: Reviews, 2010. **16**(5): p. 523-539.
6. Melchels, F.P.W., et al., *Mathematically defined tissue engineering scaffold architectures prepared by stereolithography.* Biomaterials, 2010. **31**(27): p. 6909-6916.
7. Kebede, M.A., et al., *Stereolithographic and molding fabrications of hydroxyapatite-polymer gels applicable to bone regeneration materials.* Journal of the Taiwan Institute of Chemical Engineers, 2018. **92**: p. 91-96.
8. Dong, P.L., et al., *The Preparation and Characterization of beta-SiAlON Nanostructure Whiskers.* Journal of Nanomaterials, 2008.
9. Seymour, V.R. and M.E. Smith, *Distinguishing between Structural Models of beta '-Sialons Using a Combined Solid-State NMR, Powder XRD, and Computational Approach.* Journal of Physical Chemistry A, 2019. **123**(45): p. 9729-9736.
10. Altun, A., et al., *Dense, Strong, and Precise Silicon Nitride-Based Ceramic Parts by Lithography-Based Ceramic Manufacturing.* Applied Sciences, 2020. **10**: p. 996.
11. Li, Y., et al., *Osteogenic differentiation of mesenchymal stem cells (MSCs) induced by three calcium phosphate ceramic (CaP) powders: A comparative study.* Materials Science and Engineering: C, 2017. **80**: p. 296-300.
12. Schmidleithner, C., et al., *Application of high resolution DLP stereolithography for fabrication of tricalcium phosphate scaffolds for bone regeneration.* Biomedical Materials, 2019. **14**(4): p. 045018.
13. Ding, J., et al., *Bone loss and biomechanical reduction of appendicular and axial bones under ketogenic diet in rats.* Experimental and therapeutic medicine, 2019. **17**(4): p. 2503-2510.
14. Wu, X., et al., *Ketogenic Diet Compromises Both Cancellous and Cortical Bone Mass in Mice.* Calcified Tissue International, 2017. **101**(4): p. 412-421.
15. Bergqvist, A.G.C., et al., *Progressive bone mineral content loss in children with intractable epilepsy treated with the ketogenic diet.* The American Journal of Clinical Nutrition, 2008. **88**(6): p. 1678-1684.
16. Prabhakar, A., et al., *Acetone as biomarker for ketosis buildup capability--a study in healthy individuals under combined high fat and starvation diets.* Nutrition journal, 2015. **14**: p. 41-41.
17. DIETZ, D.D., et al., *Toxicity Sudies of Acetone Administered in the Drinking Water of Rodents.* Toxicological Sciences, 1991. **17**(2): p. 347-360.
18. Whyte, M.P., *Physiological role of alkaline phosphatase explored in hypophosphatasia.* Annals of the New York Academy of Sciences, 2010. **1192**(1): p. 190-200.
19. Bonsignore, L.A., V.M. Goldberg, and E.M. Greenfield, *Machine oil inhibits the osseointegration of orthopaedic implants by impairing osteoblast attachment and spreading.* Journal of Orthopaedic Research, 2015. **33**(7): p. 979-987.

20. Faia-Torres, A.B., et al., *Differential regulation of osteogenic differentiation of stem cells on surface roughness gradients.* Biomaterials, 2014. **35**(33): p. 9023-9032.
21. Faia-Torres, A.B., et al., *Osteogenic differentiation of human mesenchymal stem cells in the absence of osteogenic supplements: A surface-roughness gradient study.* Acta Biomaterialia, 2015. **28**: p. 64-75.
22. Poon, C.Y. and B. Bhushan, *Comparison of surface roughness measurements by stylus profiler, AFM and non-contact optical profiler.* Wear, 1995. **190**(1): p. 76-88.